ARL-TR-8681 ● Apr 2019

DEVCOM ARMY RESEARCH LABORATORY

Deblurring of X-radiographs Acquired Using 150-, 300-, and 450-kV Flash X-ray Systems: Compensation for a Finite Source Size

by Michael B Zellner and Willard Casey Uhlig

NOTICES

Disclaimers

The findings in this report are not to be construed as an official Department of the Army position unless so designated by other authorized documents.

Citation of manufacturer's or trade names does not constitute an official endorsement or approval of the use thereof.

Destroy this report when it is no longer needed. Do not return it to the originator.

ARL-TR-8681 ● APR 2019

Deblurring of X-radiographs Acquired Using 150-, 300-, and 450-kV Flash X-ray Systems: Compensation for a Finite Source Size

by Michael B Zellner and Willard Casey Uhlig
Weapons and Materials Research Directorate, CCDC Army Research Laboratory

REPORT DOCUMENTATION PAGE

Form Approved
OMB No. 0704-0188

1. REPORT DATE *(DD-MM-YYYY)*	2. REPORT TYPE	3. DATES COVERED (From - To)
April 2019	Technical Report	1 October 2018–30 March 2019

4. TITLE AND SUBTITLE
Deblurring of X-radiographs Acquired Using 150-, 300-, and 450-kV Flash X-ray Systems: Compensation for a Finite Source Size

5a. CONTRACT NUMBER

5b. GRANT NUMBER

5c. PROGRAM ELEMENT NUMBER

6. AUTHOR(S)
Michael B Zellner and Willard Casey Uhlig

5d. PROJECT NUMBER

5e. TASK NUMBER

5f. WORK UNIT NUMBER

7. PERFORMING ORGANIZATION NAME(S) AND ADDRESS(ES)
US Army Combat Capabilities Development Command, Army Research Laboratory
ATTN: FCDD-RLW-PD
Aberdeen Proving Ground, MD 21005-5069

8. PERFORMING ORGANIZATION REPORT NUMBER
ARL-TR-8681

9. SPONSORING/MONITORING AGENCY NAME(S) AND ADDRESS(ES)

10. SPONSOR/MONITOR'S ACRONYM(S)

11. SPONSOR/MONITOR'S REPORT NUMBER(S)

12. DISTRIBUTION/AVAILABILITY STATEMENT
Approved for public release; distribution is unlimited.

13. SUPPLEMENTARY NOTES
ORCID IDs: Michael Zellner, https://orcid.org/0000-0001-7309-312X; Willard Uhlig, https://orcid.org/0000-0003-1815-0106

14. ABSTRACT
This report looks at the capability to deblur X-radiographs that were acquired using 150-, 300-, and 450-kV flash X-ray systems to create sharper radiographic images with greater spatial resolution. The deblurring process includes compensation for image artifacts resulting from the X-ray generation across a finite area instead of from an ideal spot. To compensate for the image artifacts, we first image where the X-rays are generated on the anode using a pinhole camera. We then use this image to compute a point spread function (PSF), which is used to deconvolve the image. Because the X-ray generation is somewhat repeatable, we also construct a set of general PSFs that can potentially be used to enhance spatial resolution of previously acquired radiographic images.

15. SUBJECT TERMS
X-radiography, point spread function, deblurring, flash radiography, deconvolution

16. SECURITY CLASSIFICATION OF:			17. LIMITATION OF ABSTRACT	18. NUMBER OF PAGES	19a. NAME OF RESPONSIBLE PERSON
a. REPORT	b. ABSTRACT	c. THIS PAGE			Michael B Zellner
Unclassified	Unclassified	Unclassified	UU	24	19b. TELEPHONE NUMBER (Include area code) 410-306-2565

Standard Form 298 (Rev. 8/98)
Prescribed by ANSI Std. Z39.18

Contents

List of Figures

Acknowledgments

The authors are grateful to Dr Roarke Horstmeyer at Duke University for sharing his optical-based research and techniques, which inspired much of the research discussed here. The authors are also grateful to the members of the US Naval Research Laboratory's Pulsed Power Physics Branch within the Plasma Physics Division for collaborations and engagements concerning the X-ray source spot measurements and techniques. Those members include J Schumer, J Zier, D Hinshelwood, R Allen, D Mosher, and AS Richardson. Finally, the authors are also grateful to Dr Brady Aydelotte of the US Army Combat Capabilities Development Command, Army Research Laboratory's Armor Mechanics Branch within the Weapons and Materials Research Directorate for a technical review of this manuscript.

1. Introduction

Radiography is a useful tool for nondestructive assessment. The technique has been applied over a broad range of fields spanning medical diagnoses[1,2] to observation of mechanical system kinematics such as internal combustion within an engine.[3] Flash radiography,[4] a subset of the radiography field, extends these capabilities to situations in which sub-microsecond temporal resolution is needed to characterize dynamic events. This technique has been used extensively by experiments focusing on assessment of dynamics and materials' responses during events like ballistic impacts and explosives' detonations.[5,6] From a diagnostic development perspective, enhancements to flash radiography techniques typically come in the form of shrinking the overall equipment size, reducing the overall equipment and analysis cost, increasing the X-ray flux, increasing the X-ray energy, achieving more efficient detection of scattered X-rays, or developing analysis methods to better utilize the information gleaned from current experimental configurations. This work focuses on the latter, specifically addressing how one can increase spatial resolution of the recovered image through application of relatively well-known image analysis techniques.

To enhance the radiographic images, we focus on analysis methods to deblur images collected using an X-ray source of a finite size. In this work, we focus on improving X-radiographs acquired with L3 Applied Technologies' (L3's) pulsed X-ray systems that were equipped with standard X-ray tubes and remote tube heads.[7] Although X-rays can scatter in various ways, we apply our corrections assuming X-rays interact in an ideal fashion with a target object to create a shadowgraph image at the detector plane (i.e., the X-rays either propagate directly to the detector, or become scattered in a manner such that they do not get to the detector at all). This is graphically represented using a ray diagram approximation (Fig. 1). When a generation source is not an ideal spot, it creates an inverted image at the detector that is blurred by a factor related to the finite dimensions of the source spot and setup geometry.

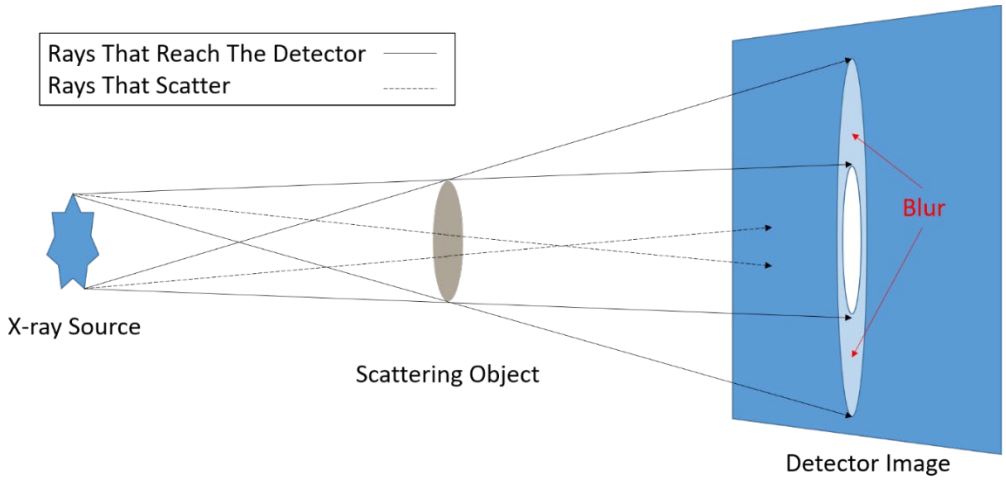

Fig. 1 Ray schematic depicting generation of image blur resulting from an X-ray source of finite dimensions

To correct for the finite X-ray source size, we can approximate the collection system as an optical system that incurs a simplistic point-spread-function (PSF). The labeling "simplistic" derives from the fact that air has an index of refraction very near 1 for electromagnetic radiation of X-ray energies.[8] The optical collection system therefore appears as a lensless inverted expansion of the geometrically finite source from a point located at the object plane (Fig. 2). Any real X-radiographic image acquired by a nonpoint-like object (such as the femur bone within the human leg) is a convolution of the PSF with the many scattering points that make up the true object. Because of this convolution, the radiographic image undergoes both broadening of spatial features and reduction of local intensities in its raw form. However, the scattering function (image) can be recovered by performing a deconvolution.

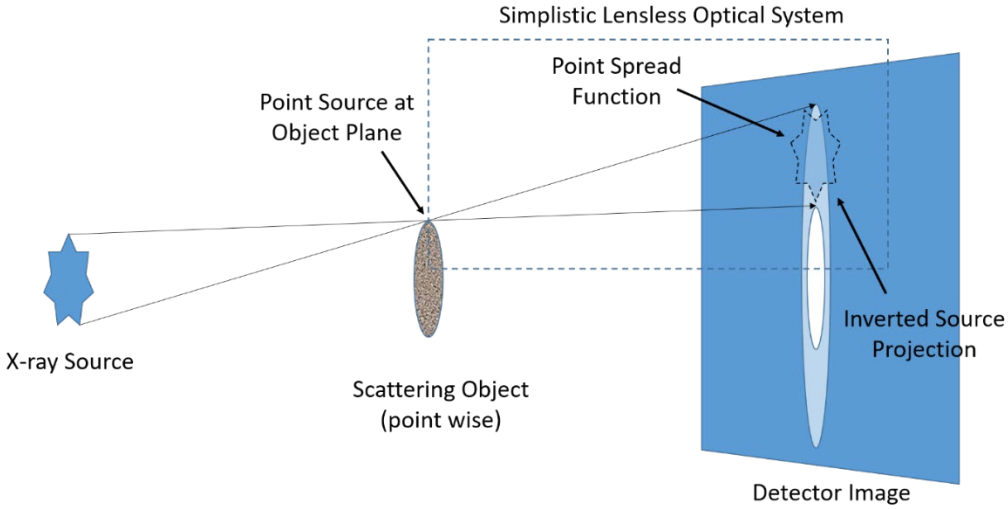

Fig. 2 X-ray collection system and comparison to a simplistic lensless optical system

To perform the aforementioned correction, one needs to know the PSF of the system. For the method we outline in this document, the PSF is computed from the X-ray source spot size, which was imaged using a pinhole camera for three pulsed X-ray systems: 150, 300, and 450 kV. Deconvolution is then performed for this PSF from projections of phantom fiducials to demonstrate spatial resolution increases. Additionally, we generated a series of approximate PSFs that are useful for postprocessing previously acquired radiographs where the source spot size and PSF are unknown.

2. Methods and Discussion

In flash radiography, X-rays are generated by discharging stored energy from a Marx generator across an anode/cathode pair (sometimes referred to as an X-ray diode) to ground. During this process, electrons that are discharged from the cathode become arrested near the anode, resulting in emission of bremsstrahlung radiation in the form of X-rays, which are used for imaging.

The first step in computing the PSFs that will be used to deblur the images is to measure the geometry of the X-ray generation spot. This can be done using a pinhole camera. Figure 3 shows a schematic of the pinhole camera setup in relation to the X-ray tube, the tube head, and X-ray generation process.

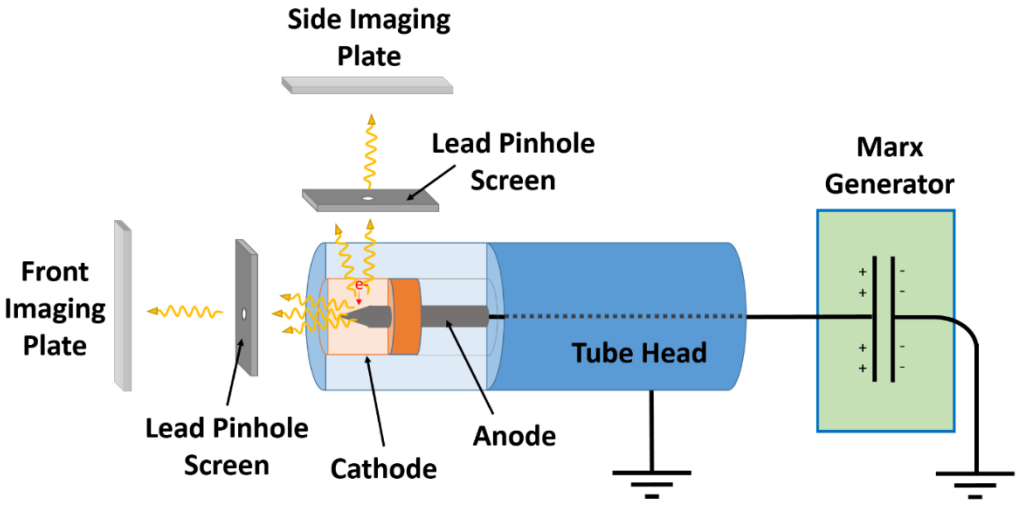

Fig. 3 Pinhole camera setup used to collect images of the X-ray source generation. This schematic shows setups for both the front and side imaging locations; however, each location was measured independently on different X-ray discharges.

To become more familiar with the L3 geometry of the anode/cathode pair, Fig. 4 shows X-radiographs of three L3 X-ray tubes that are used in the L3 150-, 300-, and 450-kV systems. The anodes are of pencil-like pointed-rod geometry for all

three systems, while the cathodes take the form of rings or washers surrounding the pointed tip of the anode. In the 300- and 450-kV tube designs, a set of rings extend toward the anode instead of a singular ring, which is used in the 150-kV system. These features are indicative of the most likely region where electrons will jump from the cathode to the anode, becoming the likely origin for X-ray emission. The rings are highlighted by red arrows superimposed on Fig. 4.

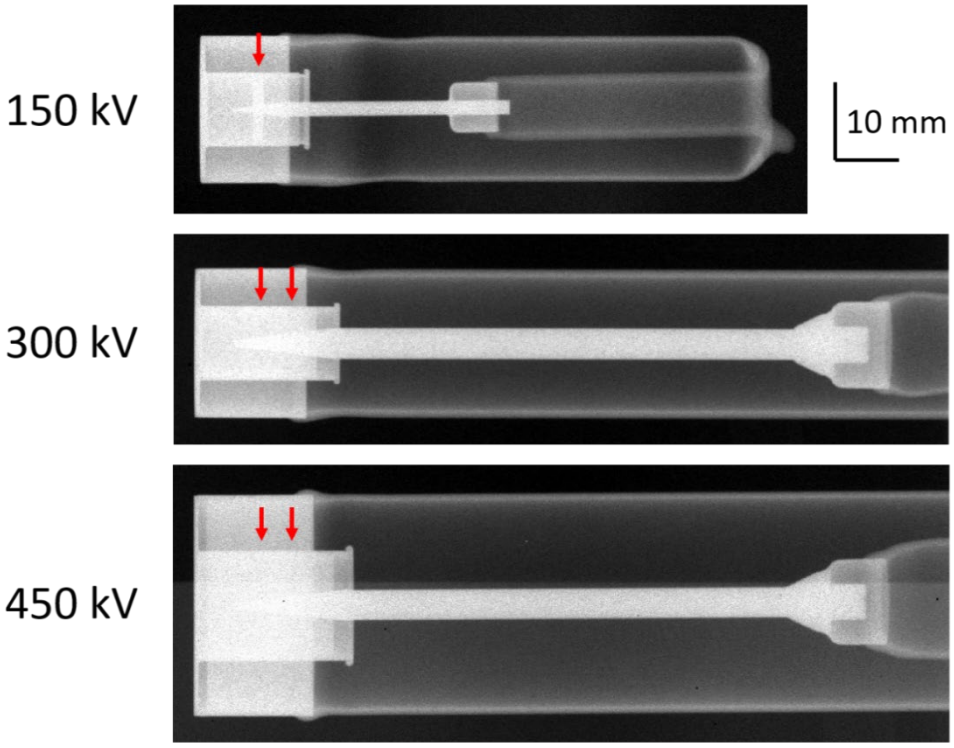

Fig. 4 X-radiographs of L3's 150- (top), 300- (middle), and 450-kV (bottom) X-ray tubes that contain the anode/cathode pairs. The tungsten anodes take the form of a pencil-like pointed rod. The cathode surrounds the anode and has rings or washers that extend to provide a closest location to the anode. This region is likely near where the electrons will jump from the cathode to the anode. The ring in the 150-kV system tube is visible via the radiograph, but those in the 300- and 450-kV tubes are not. Overlaid red arrows indicate the ring positions for all systems.

Figure 5 shows a photograph of the lead pinhole screen, and the frontal- and side-view setups used to collect images of the X-ray generation for the 150-kV system. The lead pinhole screen was constructed by drilling a 1-mm-diameter hole through a 265- × 300-mm sheet of 2-mm-thick lead roof flashing.* This screen was taped to a 265- × 300- × 60-mm piece of 9-lb/ft^3 extruded polystyrene foam for robustness. The foam had a 13-mm hole through its thickness, which was placed coincident

* A smaller pinhole would have provided a more accurate measurement of the PSF. The 1-mm size was selected for convenience of construction. Errors incurred by this relatively large pinhole are assumed to be minimal, as a generic PSF is shown to perform sufficiently well with the deconvolution process (described later in the Results and Discussion section).

with the 1-mm hole in the lead screen so as not to scatter the X-rays propagating through the pinhole.

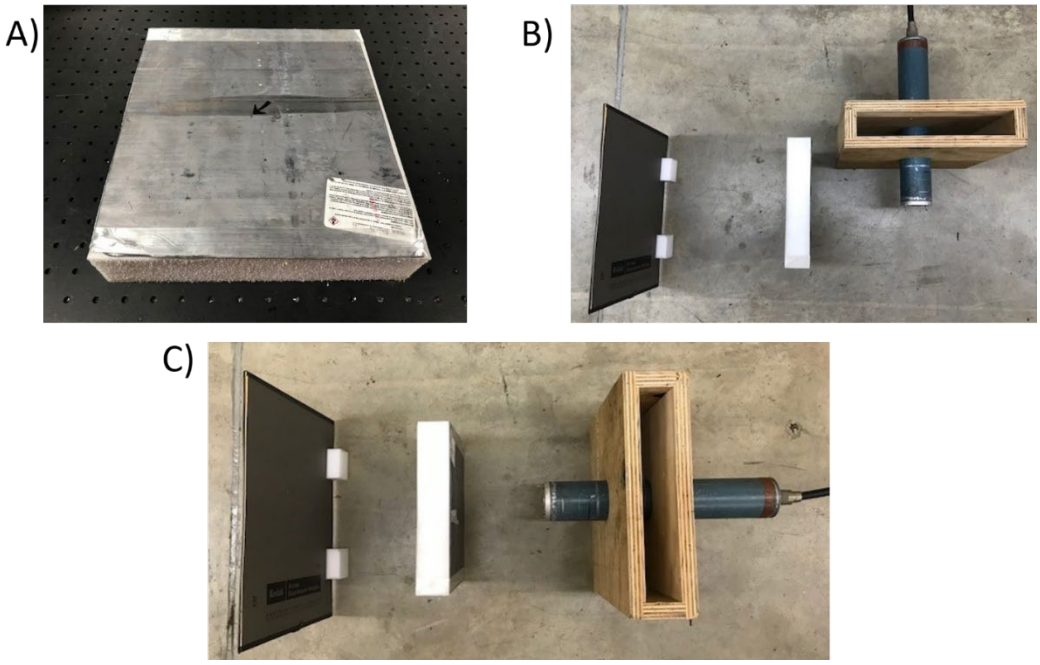

Fig. 5 A) Pinhole screen, B) side setup used to collect images of the 150-kV source generation, and C) frontal setup used to collect images of the 150-kV source generation. In A), 1-mm-diameter pinhole is located near the tip of the black arrow. In B) and C), blue tubes are the X-ray system tube head and gray rectangles are the X-ray detectors, which include a single 14- × 17-inch Carestream Health Blue HR digital imaging plate housed in a paper-based light cover.

To collect the frontal-image views, the lead pinhole screen was located along the symmetry axis of the X-ray tube at an offset of 150 mm from the location where the cathode is closest to the anode (i.e., the likely X-ray emission origin). The detector was offset 300 mm from the pinhole screen, giving a magnification factor of 2. During collection of the side views, the lead pinhole screen was offset 190 mm from the tube head symmetry axis and the imaging-plate detector was offset 265 mm from the pinhole screen, resulting in a magnification factor of 1.39. For all measurements, X-rays were collected using a Carestream Health (Rochester, New York) Blue HR digital imaging plate detector. This detector was wrapped in a paper-based light screen to prevent exposure and degradation of signal during transit to a scanner. The digital imaging plates were scanned with a Carestream Health HPX-1 scanner and images were stored in a 16-bit format for further processing.

Figure 6 shows the frontal- and side-view projections of the X-ray sources collected with the pinhole camera for the 150-, 300-, and 450-kV systems. Because the side

views collected less flux, 10 flashes were integrated to create the side-view images. For this reason, the side-view images should only be used to perceive a general location where the X-rays are generated. The frontal-view images used a single flash. These results indicate that discharge of electrons from the cathode tend to localize on the anode and, therefore, generate X-rays from an asymmetric distribution for all configurations. This effect is most significant on the 150-kV system, where X-rays appear to generate from a singular spot on one side of the pointed anode. For the 300- and 450-kV sources, the generation is less of a spot and more distributed around the anode surface. For reference, scaling of the 450-kV image indicates that most of the X-rays are generated inside a circular diameter of approximately 6 mm.

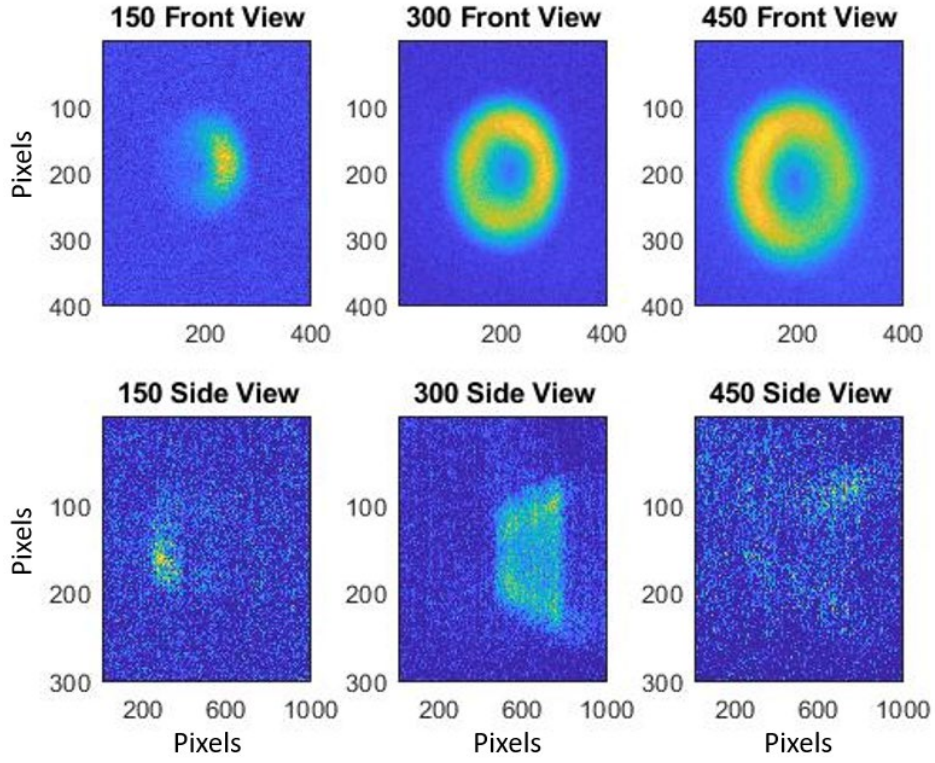

Fig. 6 Front- and side-view projections of the X-ray spot dimensions collected using the pinhole camera. The projections were collected from L3 150-, 300-, and 450-kV systems. The front-view projections were collected from a single flash. The side-view projections integrated 10 flashes to produce the projections. The dynamic range of each image was individually set to optimize the spatial reference from which X-rays are generated (both the floor and ceiling). No conclusions regarding source brilliance should be drawn comparing relative image intensities.

Figure 7 shows a comparison of front-view images of the X-ray spots from the 150-kV system collected from a single flash, and from an integration of 10 flashes. The broadening and relative shift of the most intense generation implies that the localization of electrons is imparting on the anode shifts for each individual flash.

This is not surprising considering the anodes are known to erode over time from associated ablation and thermal degradation, which alters the anode/cathode geometry relationship.

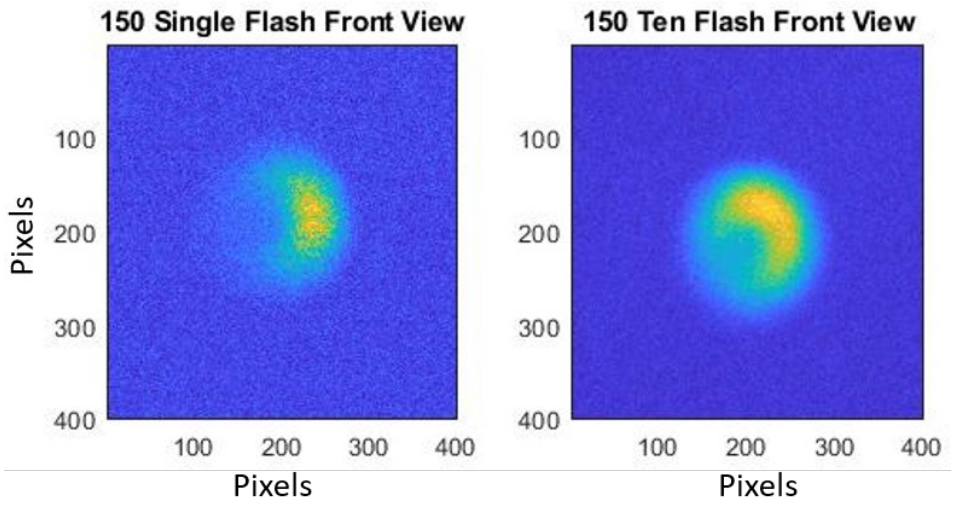

Fig. 7 Comparison of the X-ray source dimensions from a single flash with that from an integration of 10 flashes from the L3 150-kV flash system. The dynamic range of each image was individually set to optimize the spatial reference from which X-rays are generated (both the floor and ceiling). No conclusions regarding source brilliance should be drawn comparing relative image intensities.

Because of the simplistic lensless collection system geometry depicted in Fig. 2, the end-on single-flash images of the X-ray sources shown in Fig. 6 are very similar to the PSFs desired to perform a deconvolution of acquired X-ray images and enhance the image resolution. To convert the source measurements into the PSF's, the following assumptions are made:

1) The object-to-source and detector-to-object separation distances are much larger than the distance over which the X-rays are generated (indicated by the side-view pinhole projections) and, therefore, the X-ray generation is assumed to occur over a 2-D plane orthogonal to the X-ray system anode (i.e., as depicted in the front-view pinhole projections).

2) The object-to-source and detector-to-object separation distances are much larger than the dimensions of the object and, therefore, the X-ray PSFs are common across the target dimensions.

3) The angles of X-ray propagation are small and, therefore, the X-ray PSFs are common across the image field of view.

Using these assumptions, only size-scaling adjustments and normalization to unity are required to create PSFs out of the X-ray source images.

To demonstrate the deblurring capability, an X-radiograph of a Leeds test object (CN59372) was acquired using a 450-kV system. Generally, the test object was a 0.2-mm-thick screen with numerous line-pair per millimeter (lp/mm) spacings, varying from 0.25–2.5 lp/mm. The X-radiograph was captured using a Carestream GP digital imaging plate, which was scanned into a 16-bit grayscale file using a Carestream HPX-1 scanner set to a 50-μm scanning resolution. An optical photograph of the Leeds test object is shown in Fig. 8.

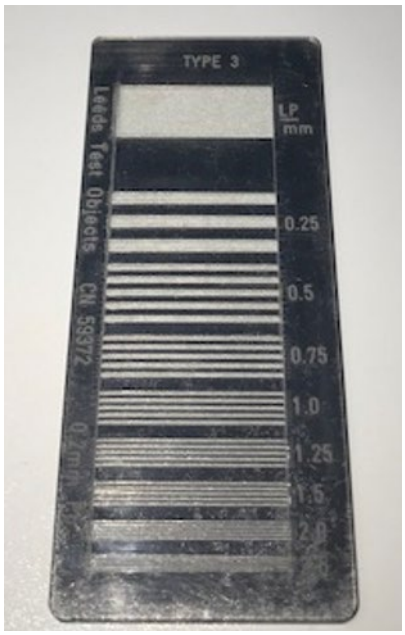

Fig. 8 Optical photograph of Leeds test object CN59372

In the demonstration experiment, the source-to-object and the object-to-detector distances were each 1 m. The resultant image used a pixel size of 50 μm/pixel, so an approximately 6-mm source dimension should project to 6 mm (or 120 pixel) PSF using the 1× magnification factor geometry. The MATLAB[9] imresize function was used to resize the PSF images (collected with a 2× magnification factor and different geometry), and the MATLAB imcrop function was used to crop the PSF image to isolate the region of illumination (ensuring the extending region is identically zero and does not include background noise). This image was then normalized to unity for ease of mathematical implementation. Figure 9 shows the PSF generated from the frontal source image (Fig. 6, top row) that is used to deconvolve the Leeds 450-kV X-ray image.

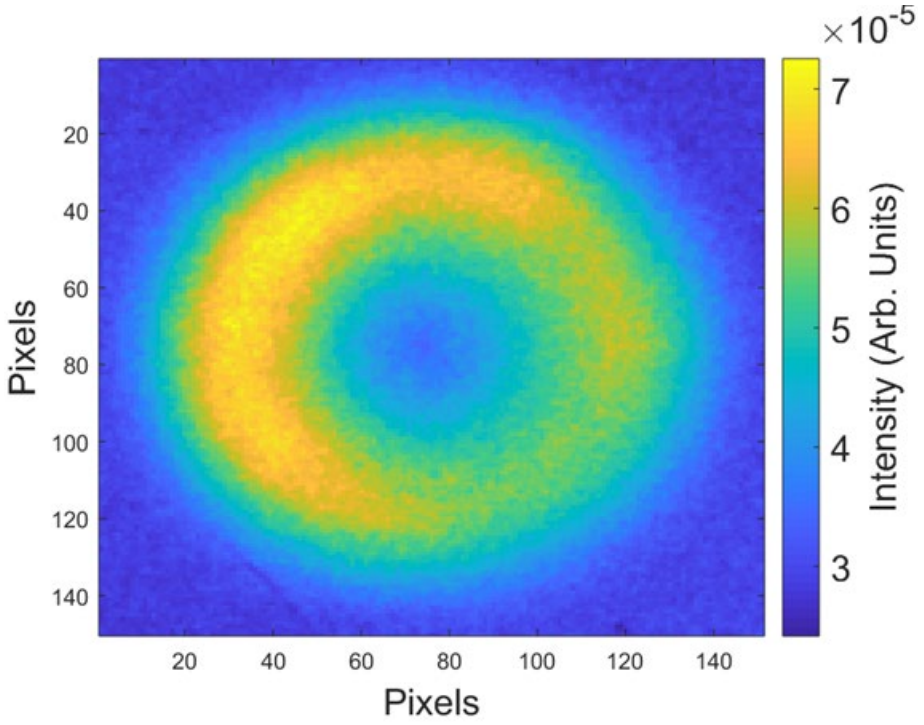

Fig. 9 PSF calculated from pinhole image data of the 450-kV L3 X-ray systems. This PSF was calculated for a 1-m source-to-object distance and a 1-m object-to-detector distance.

The unmodified radiograph of the Leeds object, along with a lineout of the dynamic range, is shown in Fig. 10. At first glimpse, a spacing of 0.5 lp/mm appears capable of being resolved. However, comparison of the optical image and the radiographic results indicate that only four of the five transmission areas are capable of being resolved. Also, at this resolution, the dynamic range did not recover 100% transmission (a value of 760 intensity in arbitrary units [A.U.] with a baseline of approximately 320 A.U.), but rather only 50% (570 A.U.).

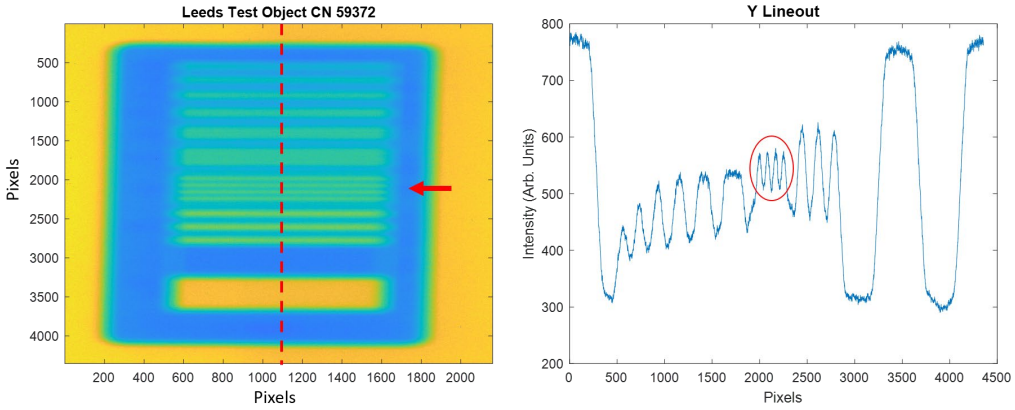

Fig. 10 X-radiograph and lineout of the Leeds test object as extracted assuming a point X-ray source. The lineout is extracted from the region indicated by the superimposed dashed red line. The red arrow and red circle highlight the region where the Leeds test object has 0.5 lp/mm fiducial spacing.

Figure 11 shows the same experiment after performing a deblur deconvolution using MATLAB's deconvwrn function and the PSF computed in Fig. 9. This method is a Fourier-transform-based method, which reduces the processing time by shifting the deblur mathematics from a direct deconvolution to a simple multiplication in Fourier space. The deblur deconvolution was accomplished using the following steps:

1) Ringing that will be introduced by the discrete Fourier transform was compensated for by using MATLAB's edgetaper function.

2) A deblur deconvolution was performed using MATLAB's deconvwrn function, the edgetaper output, and the image noise (approximated as 0.01).

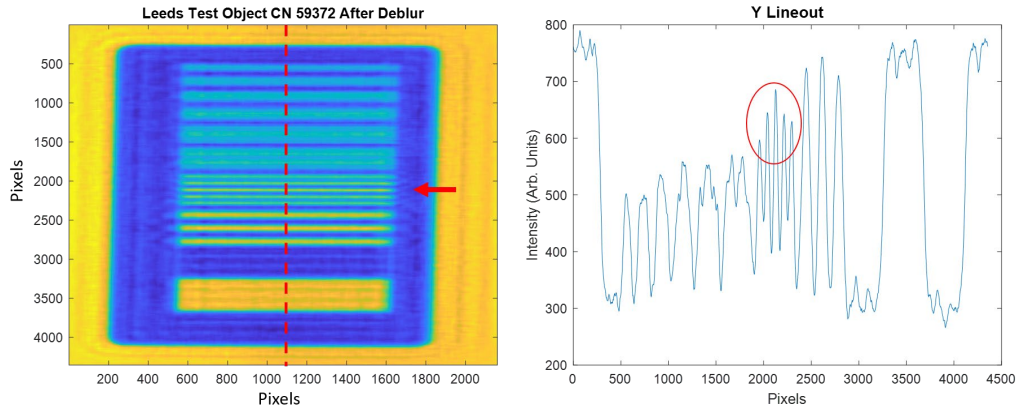

Fig. 11 X-radiograph and lineout of the Leeds test object after a deblur deconvolution was performed using the PSF shown in Fig. 7. The lineout is extracted from the region indicated by the superimposed dashed red line. The red arrow and red circle highlight the region where the Leeds test object has 0.5 lp/mm fiducial spacing.

After the deblur deconvolution, all five transmission regions are capable of being discerned within the 0.5 lp/mm region. Also, a significant portion transmission was recovered within the expected no-material regions, approaching transmission levels near 85%. Small errors likely occur from extrapolation of the PSF calculated from measurement of the 450-kV system spot on a separate experiment from that on which the analysis was performed, as the spot is known to vary from experiment to experiment (see Fig. 6).

Figure 12 shows a similar deblur deconvolution analysis of the experiment, but instead of computing the PSF from a measured source, an artificially created disk-shaped PSF was used.* The disk-shaped PSF was created using MATLAB's fspecial routine with "disk" shape and radius similar to that measured from the source (approximately 6 mm diameter). The disk shape had uniform value interior to the disk radius, and zero value external to the disk radius. Although utilization of this artificially constructed PSF was not quite as successful as the doughnut-shaped measured typical PSF, it did significantly enhance both the spatial resolution of the image and the contrast near edge features. Once again, all five transmission regions were capable of being resolved. Similar recovery was capable using a Gaussian-shaped PSF where the full-width at half-maximum value was set to three-quarters the disk diameter.

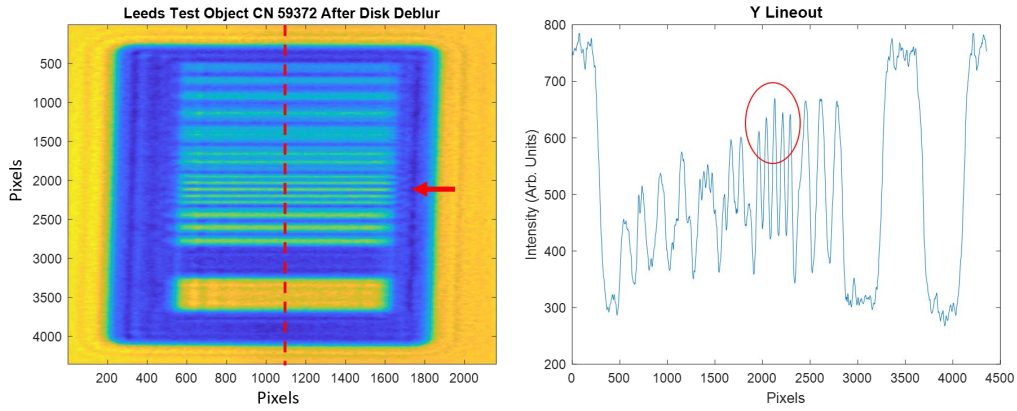

Fig. 12 X-radiograph and lineout of the Leeds test object after a deblur deconvolution was performed using a generic disk-shaped PSF of approximately 6 mm in diameter. The lineout is extracted from the region indicated by the superimposed dashed red line. The red arrow and red circle highlight the region where the Leeds test object has 0.5 lp/mm fiducial spacing.

* Alternate PSF shapes, including a doughnut and a 2-D Gaussian, produced similar results. The disk-shaped PSF was chosen as a representative case because of its simplicity.

3. Conclusions

This work looks at the capability to deblur X-radiographs that were acquired using L3 150-, 300-, and 450-kV flash X-ray systems to create sharper radiographic images with greater spatial resolution. The deblurring process includes compensation for image artifacts resulting from the X-ray generation across a finite area instead of from an ideal spot. To compensate for the image artifacts, we first imaged where the X-rays are generated on the anode using a pinhole camera. We then use this image to compute a PSF. The PSF was in turn used to deconvolve the image assuming a simplistic lensless geometry. We demonstrated an example of the process using radiographs of a Leeds phantom test object. The results show that significant spatial and contrast enhancements can be gained by performing the deconvolution using both an experimentally bounded PSF and a generic artificially generated disk PSF. The latter is of significance in that it demonstrates the ability to postprocess legacy data acquired with L3 systems to possibly enhance both the spatial resolution and contrast, in which little knowledge is known about the actual spot size and shape for the particular experiment.

4. References

1. Doi K. Diagnostic imaging over the last 50 years: research and development in medical imaging science and technology. Phys Med Biol. 2006;51(13):R5-27.

2. Pines JM. Trends in the rates of radiography use and important diagnoses in emergency department patients with abdominal pain. Med Care. 2009;47(7):782–786.

3. Kastengren AL, Tilocco FZ, Duke D, Powell CF, Zhang X, Moon S. Time-resolved X-ray radiography of sprays from engine combustion network spray a diesel injectors. Atomization Sprays. 2014;24(3):251–272.

4. Germer R. X-ray flash techniques. J Phys E: Sci Instrum. 1979;12:336.

5. Webster EA. Flash X-ray studies of ballistic phenomena. In: Endelman LL, editor. Proc. SPIE 0348. 15th Intl Congress on High-Speed Photography and Photonics; 1983 Aug 21–27; San Diego, CA. Bellingham (WA): International Society for Optics and Photonics; c1983. p. 682–687. https://doi.org/10.1117/12.967819.

6. McAfee JM, Asay B, Campbell AW, Ramsay JB. The deflagration-to-detonation transition in granular HMX. Presented at: Research Center for Energetic Materials Open Seminar on Safety and Hazards Evaluation; 1991 Apr 9; New Mexico Tech, Socorro, NM. Los Alamos (NM): Los Alamos National Laboratory; c1991. Report No.: LA-UR-91-2103.

7. L3 industrial radiography solutions. San Leandro (CA): L3 Applied Technologies. [accessed 2018 Dec 28]. https://www2.l3t.com/ati/solutions/irs.htm.

8. Rumble JR, editor. CRC handbook of chemistry and physics. 99th ed. (internet version). Boca Raton (FL): CRC Press, Taylor and Francis Group; c2018 [accessed 2018 Dec 28]. http://hbcponline.com/.

9. MATLAB. Ver. 9.3. R2017b. Natick (MA): The MathWorks, Inc.; 2017.

List of Symbols, Abbreviations, and Acronyms

2-D	two-dimensional
A.U.	arbitrary units
L3	L3 Applied Technologies
lp/mm	line-pair/millimeter
PSF	point spread function

1 (PDF) DEFENSE TECHNICAL INFORMATION CTR DTIC OCA

2 (PDF) CCDC ARL
IMAL HRA
RECORDS MGMT
FCDD RLD CL
TECH LIB

1 (PDF) GOVT PRINTG OFC
A MALHOTRA

1 (PDF) PEO CS CSS
SFAE CSS FP H
PM BRIDGING
D BOCK

1 (PDF) PROJECT DIRECTOR
SFAE GCS M
MAIN BATTLE TANK SYS
TECHLGY PRGM OFC
E BARSHAW

1 (PDF) PM ABRAMS
SFAE GCS HBCT S
J ROWE
R NICOL

1 (PDF) PM BFVS
SFAE GCSS BV
D SPENCER
LTC G DEAN

1 (PDF) PM GCS
SFAE GCSS W BCT
M RYZYI
T HOWIE

1 (PDF) USMC
A PURTELL
C/O B SWEDISH

1 (PDF) DEPT OF THE ARMY
CCDC AC
FCDD ACM ML
S CHICO

3 (PDF) DEPT OF THE ARMY
CCDC GVSC
C FILAR
R RICKERT
A LEE

1 (PDF) DEPT OF THE ARMY
ATEC
CSTE DTC AT SL V
D BLANKENBILLER

111 (PDF) CCDC ARL
FCDD RLW M
J BEATTY
FCDD RLW MA
J LA SCALA
D O'BRIEN
J WOLBERT
FCDD RLW MB
G GAZONAS
B LOVE
FCDD RLW MD
B CHEESEMAN
R BRENNAN
K CHO
L HOLMES
M KORNECKI
S WALSH
FCDD RLW ME
V BLAIR
S KILCZEWSKI
J LASALVIA
P PATEL
J SWAB
L VARGAS-GONZALEZ
FCDD RLW LB
J CIEZAK-JENKINS
F DELUCIA
T JENKINS
B RICE
FCDD RLW LC
K MCNESBY
T PIEHLER
B ROOS
G SUTHERLAND
FCDD RLW LE
P WEINACHT
FCDD RLW LH
J ANGEL
B AYDELOTTE
T EHLERS
E KENNEDY
L MAGNESS
C MEYER
J NEWILL
B SCHUSTER
B SORENSEN
R SUMMERS
FCDD RLW P
D LYON
J HOGGE
T VONG

FCDD RLW PA
J BALL
P BERNING
S BILYK
J CAZAMIAS
M COPPINGER
J FLENIKEN
T KOTTKE
G THOMSON
W UHLIG
A VALENZUELA
L VANDERHOEF
C WOLFE
C HOPPEL
S SATAPATHY
S WOZNIAK
FCDD RLW PC
R BECKER
T BJERKE
D CASEM
J CLAYTON
R LEAVY
S SEGLETES
A SOKOLOW
A TONGE
C WILLIAMS
FCDD RLW PD
A BARD
N BRUCHEY
R DONEY
M DUFFY
S HALSEY
M KEELE
D KLEPONIS
R MUDD
F MURPHY
D PETTY
C RANDOW
J RUNYEON
S SCHRAML
B SCOTT
K STOFFEL
G VUNNI
V WAGONER
M ZELLNER
FCDD RLW PE
P BARTKOWSKI
S BARTUS
M BURKINS
D GALLARDY
P GILLICH
D HACKBARTH
D HORNBAKER
J HOUSKAMP
T JONES
C KRAUTHAUSER
M LOVE
K MCNAB
P SWOBODA
FCDD RLW PF
N GNIAZDOWSKI
D HOFSTETTER
S HUG
C CUMMINS
D ERDMAN
R KARGUS
FCDD RLW PG
R EHLERS
B HOMAN
S KUKUCK
C PECORA
R SPINK
J STEWART
J LENHART
K MASSER